Supplementary Information for

Molecular-scale tough adhesives based on the Lake-Thomas model

Yuseon Heo[1†], Hakjun Lee[1†], Chang Seo Park[1], Jinwoo Park[1], Seounghyun Sun[1], Sunbo Kang[1], Gimin Sung[1], Yun Hyeok Lee[1,5], Byoung Soo Kim[2], Jihye Shim[3], Junhyeong Park[3], Jeong-Yun Sun[1,4]*

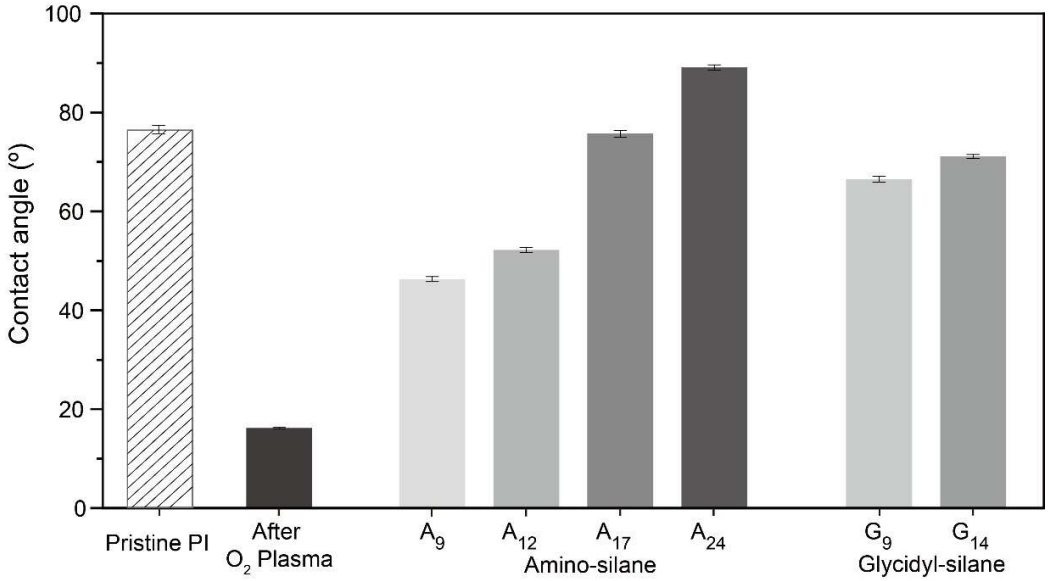
Correspondence to: jysun@snu.ac.kr

This Supplementary Information includes:

Supplementary Figs. 1 - 25
Supplementary Tables 1- 3
Supplementary Note 1-3
Supplementary References 1 - 21
Captions for Supplementary Movies 1 and 2

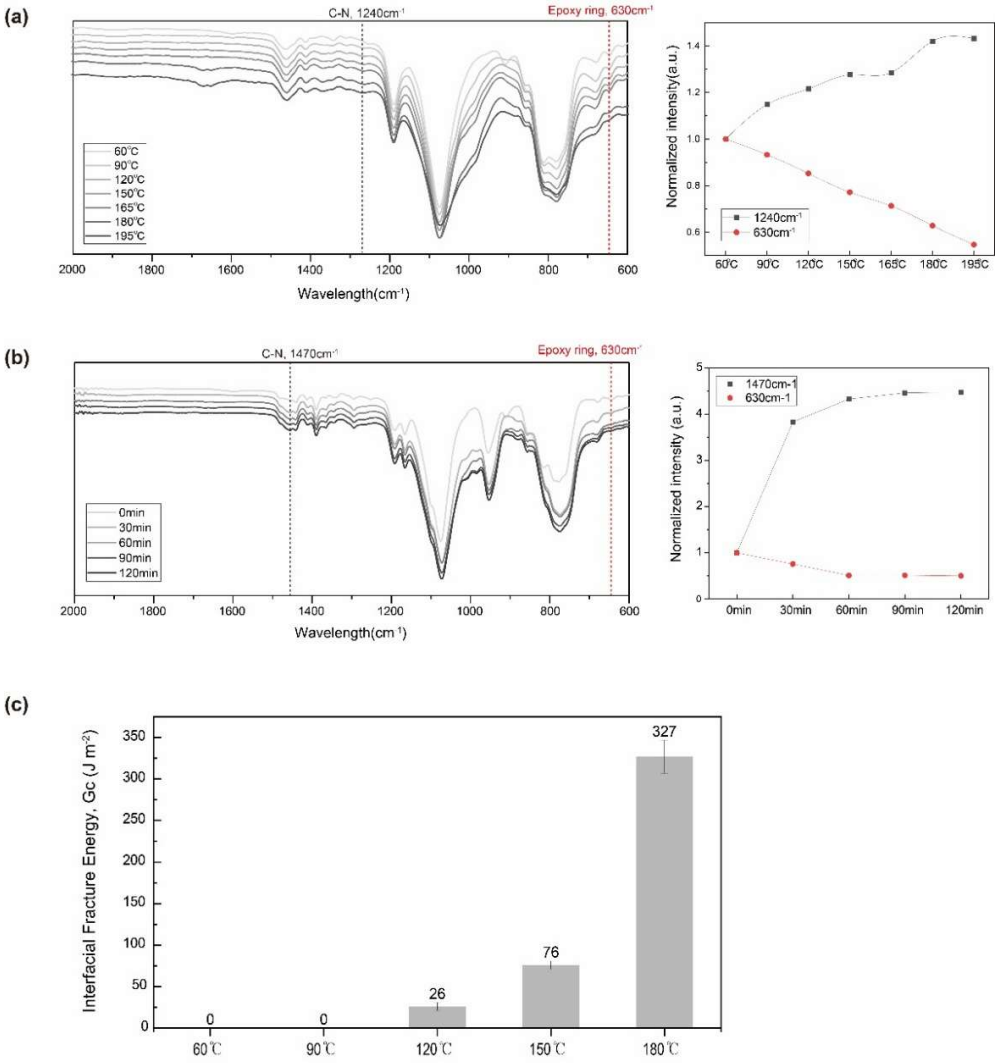
Other Supplementary Materials for this manuscript include the following:

Supplementary Movies 1 and 2



Supplementary Fig. 1 | Water contact angles of PI surfaces after plasma and silane treatments.

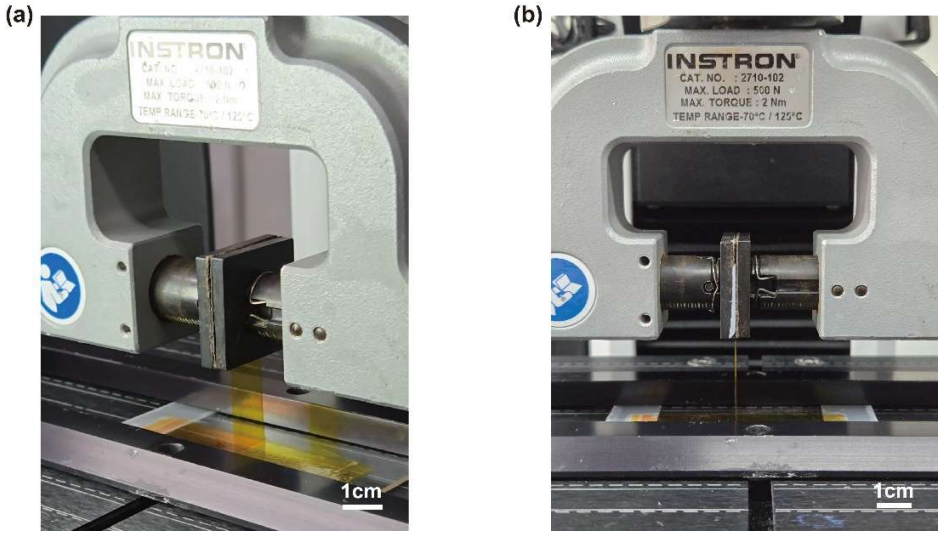
Static water contact angles of pristine PI, O_2-plasma-treated PI, and PI surfaces functionalized with amino-silanes (A_9, A_{12}, A_{17} and A_{24}) or glycidyl-silanes (G_9 and G_{14}). O_2 plasma markedly decreased the contact angle of pristine PI, whereas subsequent silane treatment increased the contact angle, with values depending on the molecular structure of the grafted silane. The distinct contact angles after silane treatment support modification of the PI surface by the respective amino- and glycidyl-silanes.



Supplementary Fig. 2 | Temperature- and time-dependent epoxy–amine coupling in a model silane system and adhesion development at PI–PI interfaces.

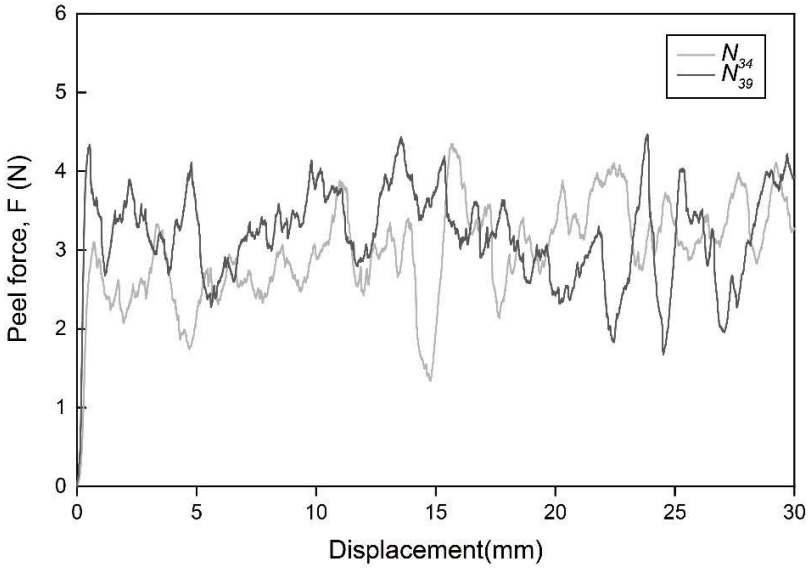
(a) FTIR spectra of a 1:1 molar mixture of APTMS and GPTMS reacted for 60 min at different temperatures, together with the normalized intensities of the C–N band at 1,240 cm^{-1} and epoxy-ring band at 630 cm^{-1}. Band intensities were normalized to the corresponding values at 60 °C. (b) FTIR spectra of the APTMS/GPTMS mixture reacted at 180 °C for different times, together with the normalized intensities of the C–N band at 1,470 cm^{-1} and epoxy-ring band at 630 cm^{-1}. Band intensities were normalized to the corresponding values at 0 min. (c) Interfacial fracture energy, G_c, of APTMS/GPTMS-functionalized PI–PI interfaces bonded at 60, 90, 120, 150 or 180 °C under 3 kPa for 1 h.

Whereas epoxy–amine coupling is detectable at relatively low temperatures in the free mixture, substantial interfacial adhesion develops only at higher temperatures in the surface-bound system, with a pronounced increase at 180 °C.



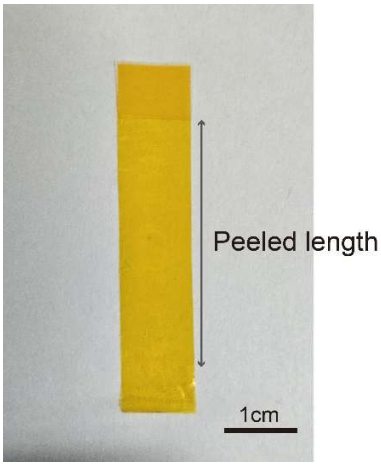
Supplementary Fig. 3 | Experimental configuration for 90° peel testing.

(a), (b) Near-frontal and oblique views of the Instron peel-test fixture during measurement. A 25-μm-thick PI film was pulled vertically as the peel arm, while the opposing bonded substrate was fixed horizontally to the lower stage, maintaining a nominal peel angle of 90°.



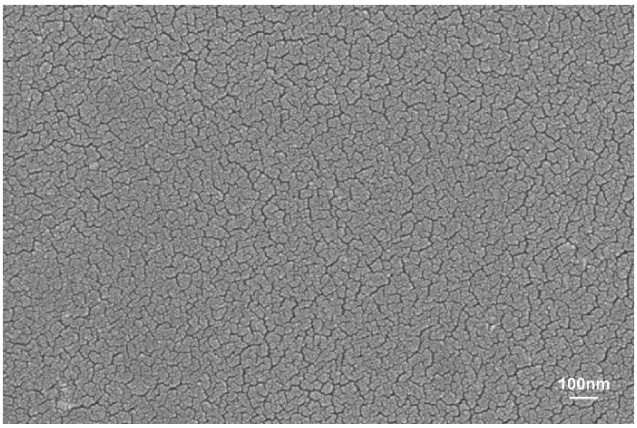
Supplementary Fig. 4 | Representative 90° peel force–displacement curves of N_{34}- and N_{39}-bonded PI–PI interfaces.

Representative peel force–displacement responses measured during 90° peel tests of PI–PI interfaces formed with N_{34} and N_{39} interlinked molecular bridges. The steady-state peel forces were used to determine the corresponding interfacial fracture energies reported in Fig. 2e.



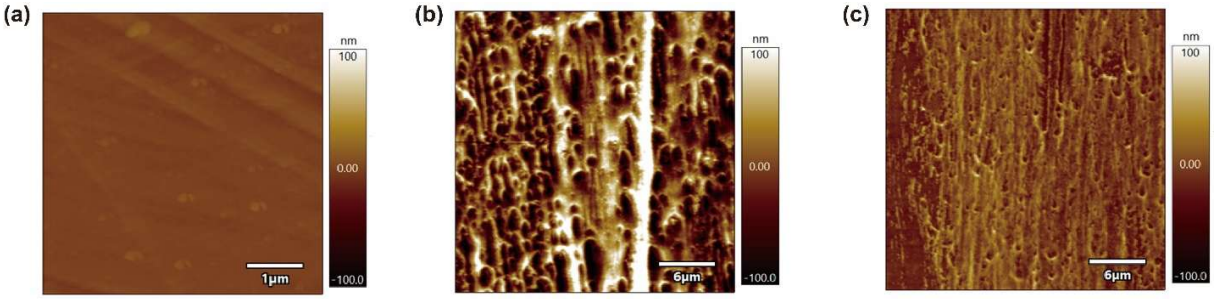
Supplementary Fig. 5 | Elastic recovery of the PI peel arm after 90° peel testing.

Representative photograph of the 25-μm-thick PI peel arm after complete unloading following 90° peel testing of an N_{32}-bonded PI–PI interface. The peeled PI film recovered a nearly flat configuration without apparent permanent curvature. The deformed peel-arm configuration during testing is shown in Supplementary Fig. 3. The contribution of peel-arm extensibility to the measured fracture energy is quantified using the Kendall peel model in Supplementary Note 1.



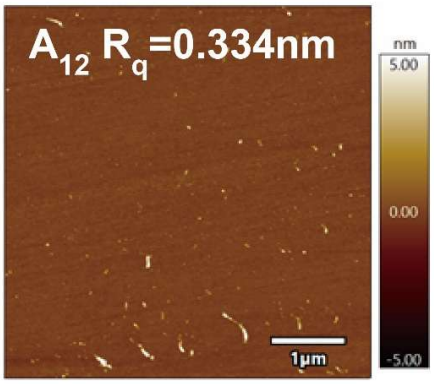
Supplementary Fig. 6 | Surface morphology of pristine PI.

Representative FE-SEM image of pristine PI before surface treatment, shown as a reference for comparison with the fracture surfaces in Fig. 2f,g. The fine surface cracking visible in the image originates from the Pt coating applied for SEM observation rather than from the intrinsic PI surface morphology.



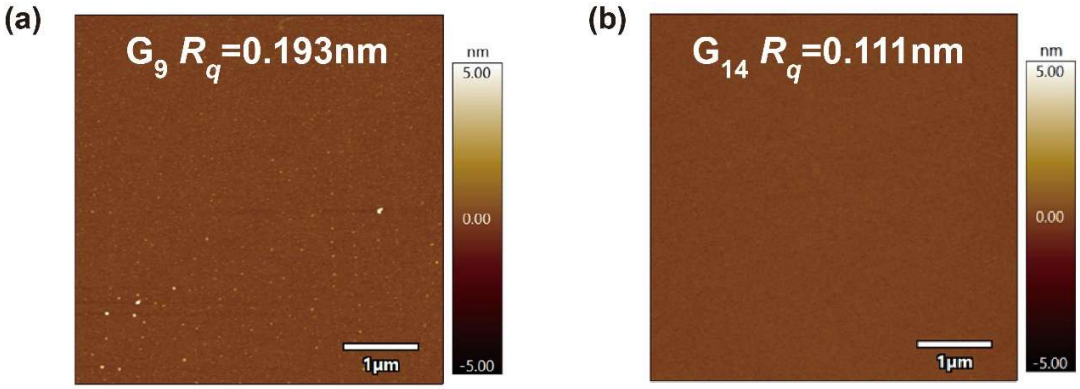
Supplementary Fig. 7 | 2D AFM topography of pristine and peeled PI surfaces.

Representative 2D AFM height images of (a) pristine PI, (b) the top-PI fracture surface and (c) the bottom-PI fracture surface after 90° peeling of the N32-bonded PI–PI interface. The corresponding root-mean-square surface roughness, R_q, was 6.4, 54.7 and 25.9 nm, respectively. The pronounced roughening of the fracture surfaces is consistent with the polymer deformation and material transfer observed by SEM in Fig. 2f,g. The corresponding 3D AFM topographies are shown in Fig. 2i–k.



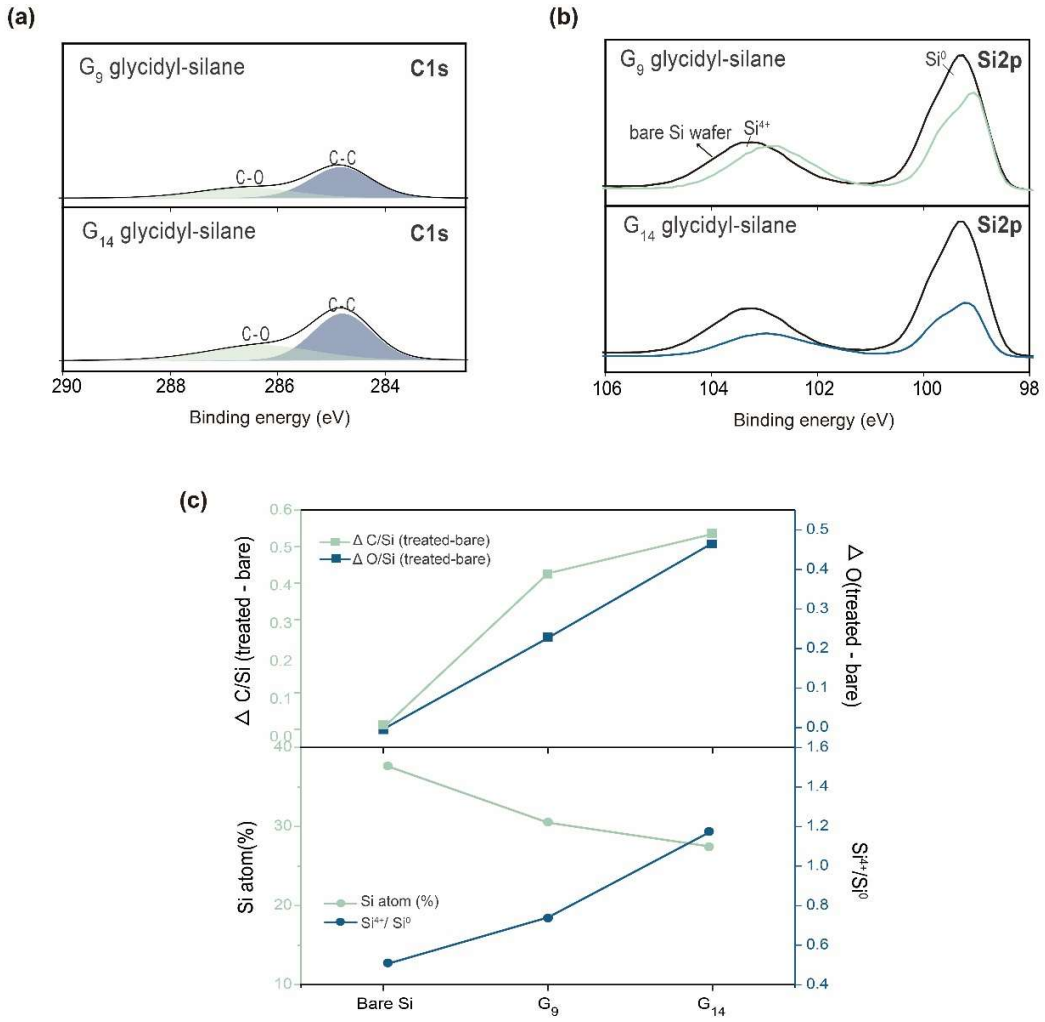
Supplementary Fig. 8 | Surface topography of an A_{12}-functionalized Si wafer.

Representative AFM height image of an A_{12}-functionalized Si wafer, showing a smooth surface with a root-mean-square roughness (*R*q) of 0.334 nm.



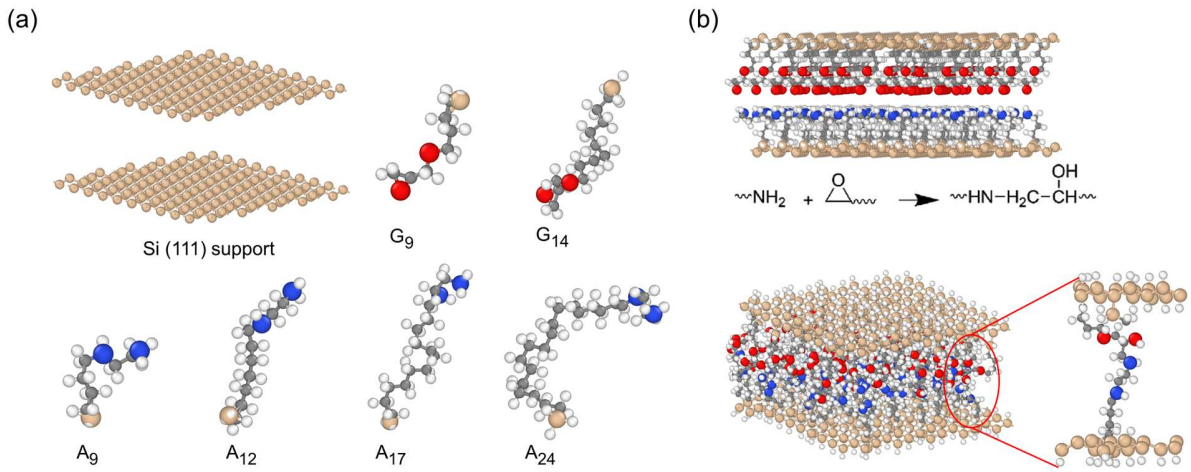
Supplementary Fig. 9 | Surface topography of glycidyl-silane-modified Si surfaces.

Representative AFM height images of Si surfaces functionalized with (a) G_9 and (b) G_{14}. The average surface roughness, R_a, was 0.193 nm for G_9 and 0.111 nm for G_{14}.



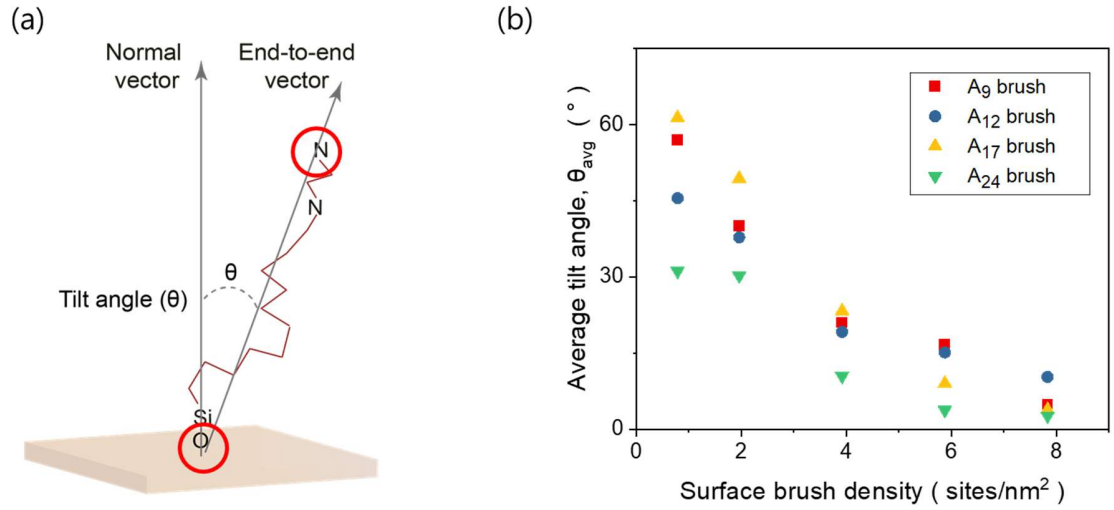
Supplementary Fig. 10 | XPS analysis of glycidyl-silane-modified Si surfaces.

a, C 1s spectra of Si surfaces functionalized with G_9 and G_{14}, showing the C–C and C–O components associated with the glycidyl-silane layers. b, Si 2p spectra of bare Si and G_9- and G_{14}-modified Si surfaces, showing the substrate-derived Si^0 and oxidized Si^{4+} contributions. c, Quantitative comparison of the changes in C/Si and O/Si ratios relative to bare Si, Si atomic fraction, and Si^{4+}/Si^0 ratio. From G_9 to G_{14}, the carbon- and oxygen-derived signals increase, whereas the substrate Si contribution decreases and the Si^{4+}/Si^0 ratio increases, consistent with increased effective surface coverage of the glycidyl-silane layer.



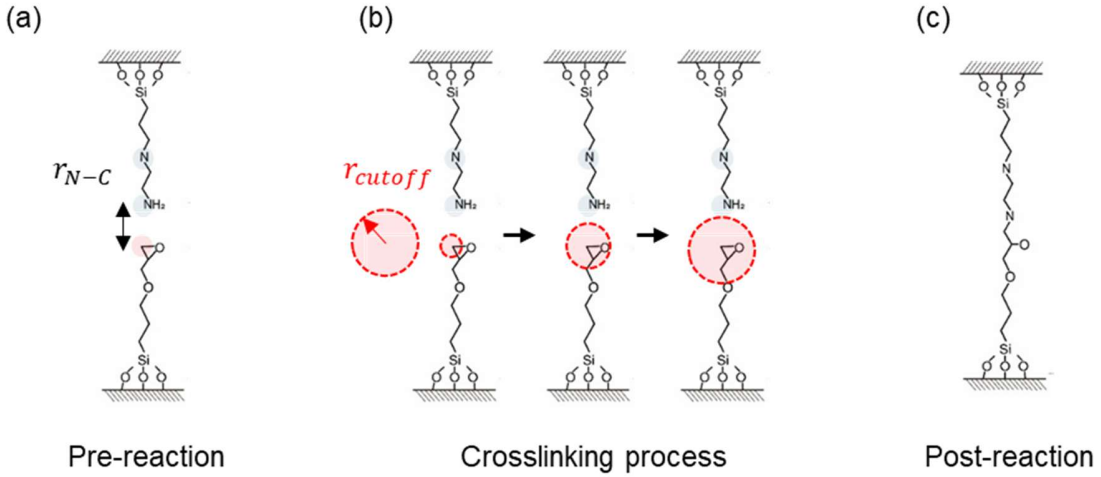
Supplementary Fig. 11| Construction of the molecular dynamics models for interlinked molecular bridges.

(a) Rigid Si (111) supports and molecular structures of the amino-silane and glycidyl-silane brushes used in the simulations. Representative configurations of the opposing amino-silane and glycidyl-silane brush layers before interfacial crosslinking. (b) Representative interlinked interface formed through epoxy–amine crosslinking between the opposing brush layers.



Supplementary Fig. 12 | Brush-density-dependent orientation of amino-silane brushes.

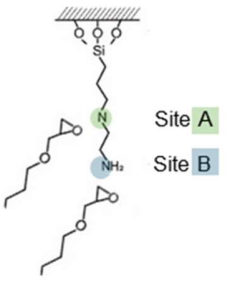
(a) Definition of the brush tilt angle, θ, measured between the surface-normal vector and the end-to-end vector connecting the surface anchoring atom to the terminal nitrogen atom of the primary amine group, each atoms are marked in red circle. An angle of 0° represents a brush oriented parallel to the surface normal. (b) Average tilt angle, θ_{avg}, as a function of nominal brush density for the A_9, A_{12}, A_{17}, and A_{24} amino-silane brushes. For each energy-minimized, uncrosslinked molecular configuration, θ_{avg} was calculated by averaging θ over all amino-silane brushes on the surface. Lower θ_{avg} indicates a more upright brush orientation relative to the surface.



Supplementary Fig. 13 | Distance-based construction of interfacial epoxy–amine bridges.

(a) Definition of a candidate epoxy–amine reaction pair between an amine nitrogen of an amino-silane brush, and a reactive epoxide-ring carbon of a glycidyl-silane brush. The interatomic distance, r_{N-C} was used to identify candidate reaction pairs in the LAMMPS fix bond/react procedure. (b) Progressive search for candidate reaction pairs by increasing the reaction cutoff, r_{cut}. A pair was selected for crosslinking when $r_{N-C} \leq r_{cut}$. (c) Representative surface-spanning bridge formed after application of the prescribed epoxy–amine reaction template.

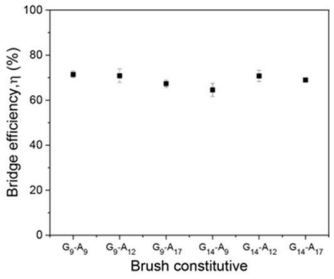
(a)



(b)

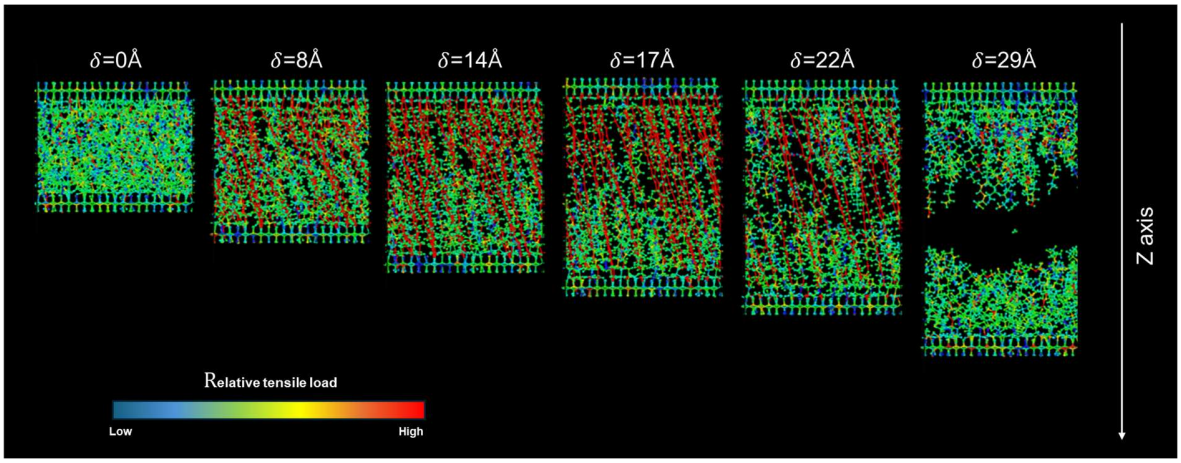
Reaction state (n_A, n_B)	Epoxy-amine linkages	Equivalent bridge units
(0,0)	0	0
(1,0)	1	1
(0,1)	1	1
(1,1)	2	1
(0,2)	2	1
(1,2)	3	1

(c)



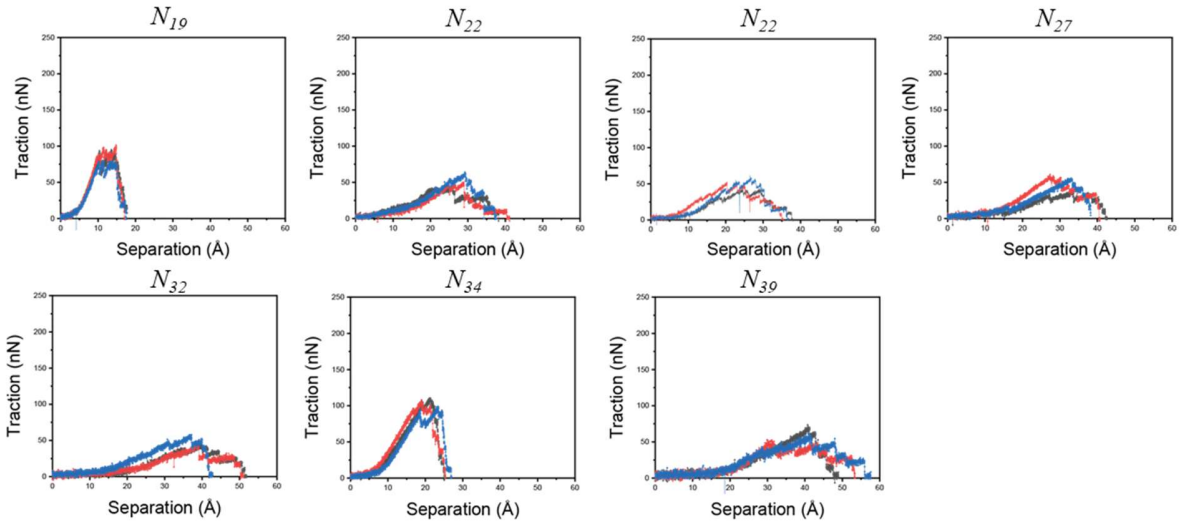
Supplementary Fig. 14 | Reaction-state classification and topology-based quantification of surface-spanning molecular bridges.

(a) Classification of the possible reaction states of a multifunctional amino-silane. The internal secondary amine and terminal primary amine were designated as sites A and B, respectively. Each reaction state was denoted by (n_A, n_B), where n_A = 0 or 1 and n_B = 0,1 or 2 represent the numbers of epoxy additions at the respective amine sites. These combinations yield six possible reaction states, including the unreacted state (0,0). (b) Topology-based counting of epoxy-amine linkages and one-to-one-equivalent surface-spanning bridge units. Each reacted amino-silane connected to the opposing surface was counted as one bridge unit, irrespective of the number of glycidyl-silane brushes attached to it. Accordingly, branched states contain multiple epoxy-amine linkages but contribute to one distinct bridge unit. The total linkage and bridge counts were calculated as $n_{link} = c_{10} + c_{01} + 2c_{11} + 2c_{02} + 3c_{12}$ and $n_{bridge} = c_{10} + c_{01} + c_{11} + c_{02} + c_{12}$, where c_{AB} is the population of amino-silanes in reaction state (n_A, n_B). (c) Realized one-to-one-equivalent surface-spanning bridge fraction for each amino-silane and glycidyl-silane combination at the target reaction conversion of 90%. The bridge fraction was calculated relative to the nominal one-to-one maximum. The topology-based bridge efficiency η, defined as n_{bridge}/n_{link} was approximately 0.70, resulting in a realized bridge fraction of approximately $0.9 \times 0.7 = 0.63$. The resulting fraction varied only weakly among the molecular combinations examined.



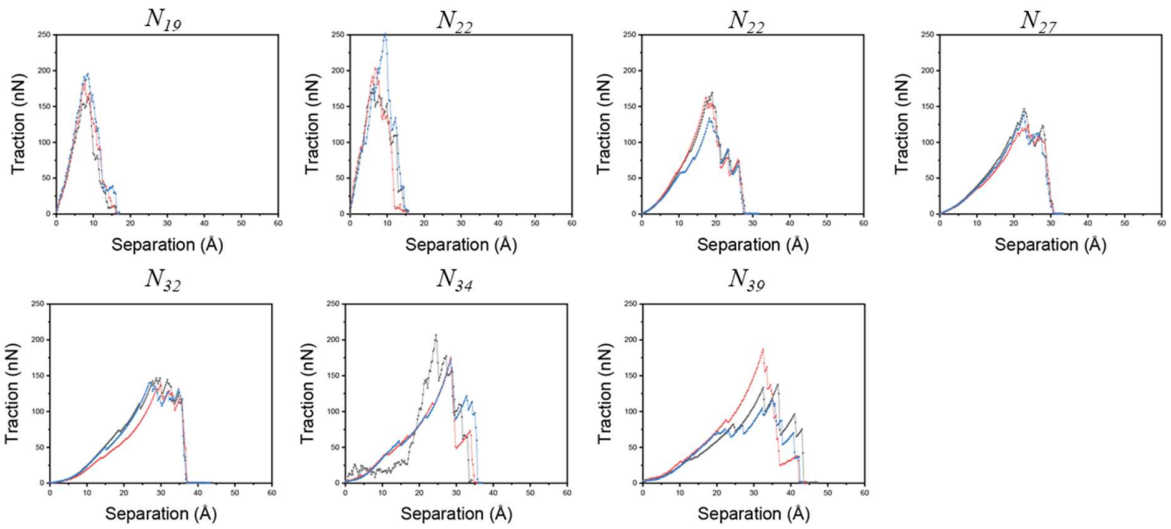
Supplementary Fig. 15 | Molecular transmission of tensile load and bond scission during separation.

Representative molecular configurations of the N_{32}, ρ_H = 3.92 sites nm^{-2} interface at increasing opening displacements, δ. As the supports were separated, the surface-spanning molecular bridges progressively elongated and transmitted tensile load along the connected molecular backbone, followed by covalent-bond scission and eventual interfacial separation. Atoms are colored according to the tensile zz-component of the per-atom virial obtained from the MD simulations. A common normalization and color scale were applied to all snapshots, with colors ranging from low to high relative tensile load. The color mapping therefore represents the relative contribution of the molecular structure to tensile load transmission rather than an absolute local stress.



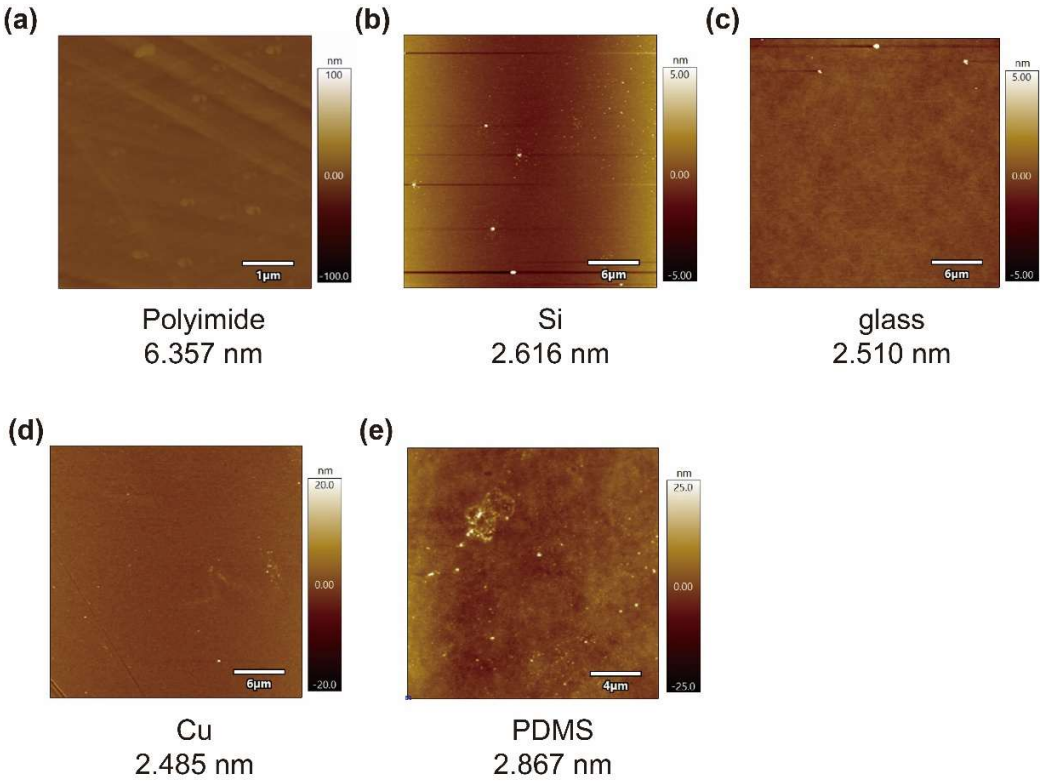
Supplementary Fig. 16 | Traction–separation responses at the low nominal brush density.

Complete force–separation curves for all bridge lengths at ρ_L = 1.96 sites nm^{-2}. Each molecular model was evaluated using three separation trajectories initiated from the same equilibrated configuration with different velocity seeds. The opening displacement was referenced to the onset of sustained tensile force.



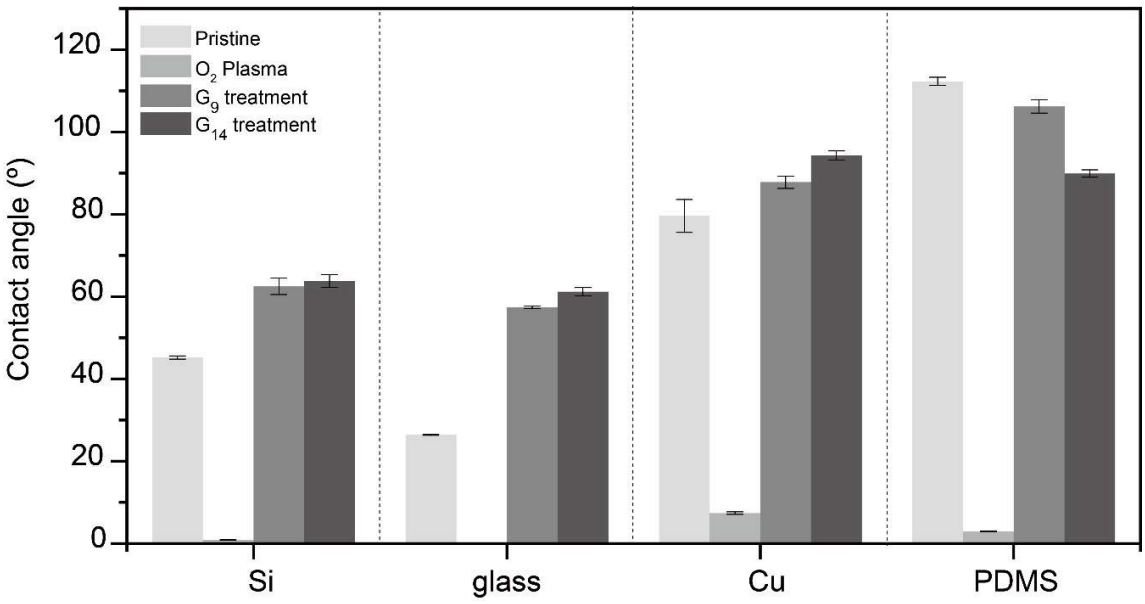
Supplementary Fig. 17 | Traction–separation responses at the high nominal brush density.

Complete force–separation curves for all bridge lengths at ρ_H = 3.92 sites nm^{-2}. Each molecular model was evaluated using three separation trajectories initiated from the same equilibrated configuration with different velocity seeds. The opening displacement was referenced to the onset of sustained tensile force.



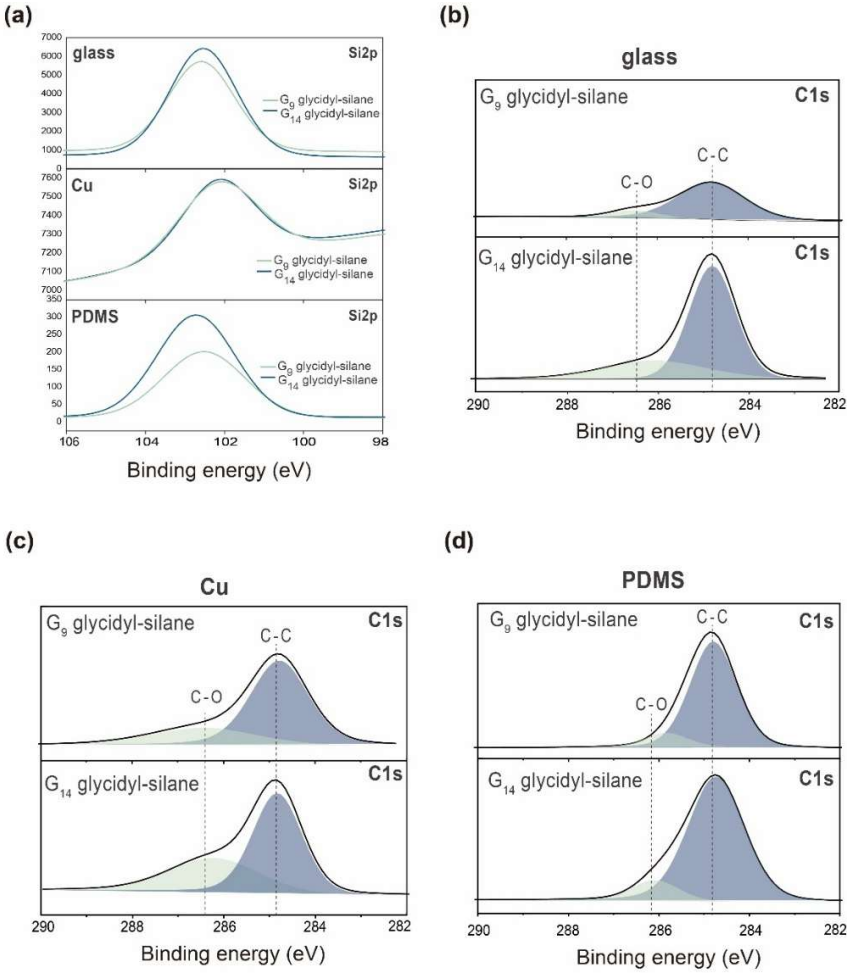
Supplementary Fig. 18 | Surface topography and roughness of the pristine substrates.

Representative AFM height images of pristine (a) polyimide, (b) Si, (c) glass, (d) Cu and (e) PDMS surfaces used for heterogeneous bonding experiments. The corresponding root-mean-square surface roughness, R_q, was 6.357, 2.616, 2.510, 2.485 and 2.867 nm, respectively.



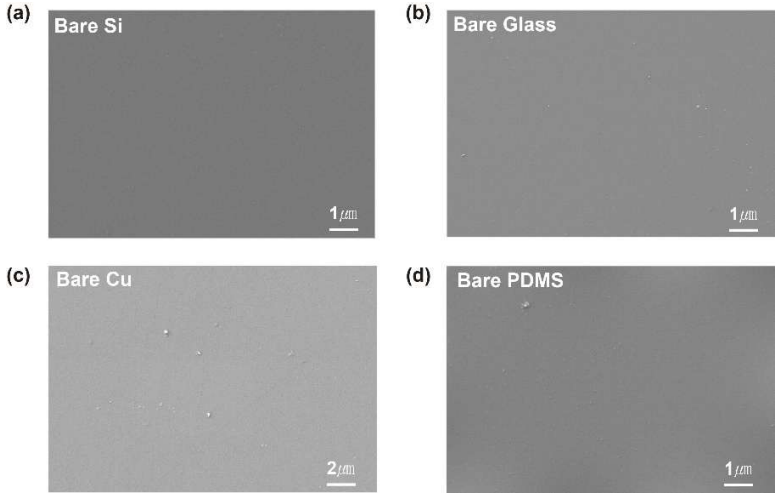
Supplementary Fig. 19 | Water contact angles of heterogeneous substrates after plasma activation and glycidyl-silane functionalization.

Static water contact angles of pristine, O_2-plasma-treated, G_9-functionalized and G_{14}-functionalized Si, glass, Cu and PDMS surfaces. O_2 plasma markedly decreased the water contact angle for all substrates, whereas subsequent G_9 or G_{14} treatment increased the contact angle relative to the plasma-treated state, consistent with modification of the activated surfaces by the glycidyl-silane layers. Data are presented as mean ± s.d. from measurements at three spatially separated positions for each condition.



Supplementary Fig. 20 | XPS characterization of glycidyl-silane-functionalized heterogeneous substrates.

(a) Si2p spectra of glass, Cu and PDMS surfaces functionalized with G_9 and G_{14} glycidyl-silanes. (b)–(d) High-resolution C1s spectra of G_9- and G_{14}-functionalized (b) glass, (c) Cu and (d) PDMS surfaces. The fitted components are assigned to C–C/C–H and C–O/C–O–C carbon environments.



Supplementary Fig. 21 | FE-SEM surface morphology of the pristine substrates used for heterogeneous bonding.

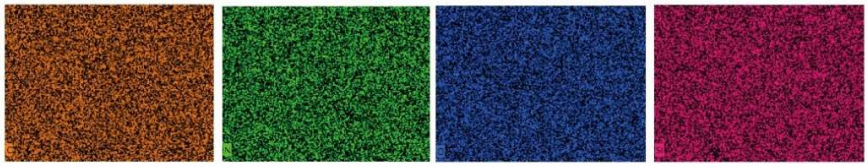
Representative FE-SEM images of pristine (a) Si, (b) glass, (c) Cu and (d) PDMS surfaces before surface treatment and bonding. These images provide baseline references for comparison with the corresponding fracture-surface morphologies after peeling in Fig. 5c–f.

(a)

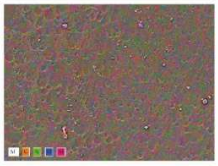
[Si-PI] Si side after peel test



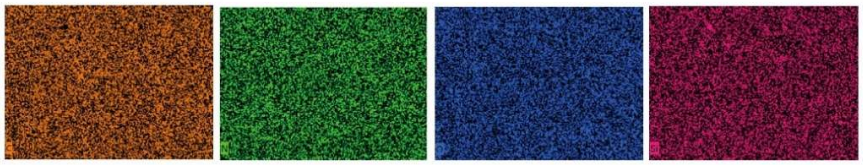
Element	At. No.	Mass [%]	Mass Norm. [%]	Atom [%]	abs. error [%]
C	6	10.20	18.53	32.65	3.23
N	7	0.54	0.97	1.47	0.24
O	8	5.03	9.14	12.09	1.64
Si	14	39.27	71.36	53.78	5.45
Pt	78	0.00	0.00	0.00	0.00
		55.04	100.00	100.00	



[Si-PI] PI side after peel test

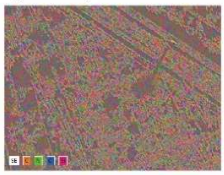


Element	At. No.	Mass [%]	Mass Norm. [%]	Atom [%]	abs. error [%]
C	6	65.86	65.56	68.77	19.26
N	7	2.85	2.85	2.69	1.18
O	8	34.59	34.59	28.54	10.96
Si	14	0.00	0.00	0.00	0.00
Pt	78	0.00	0.00	0.00	0.00
		100.00	100.00	100.00	

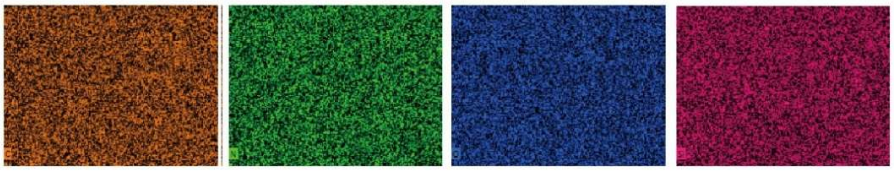


(b)

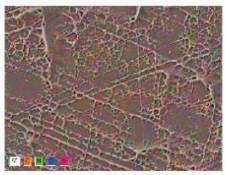
[Glass-PI] Glass side after peel test



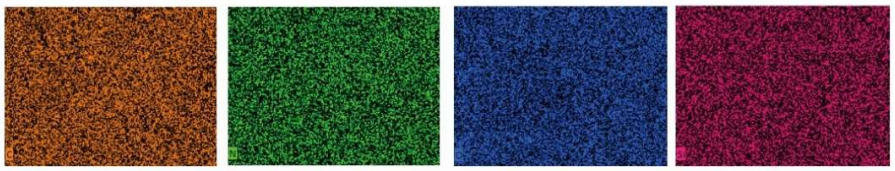
Element	At. No.	Mass [%]	ss Norm.	Atom [%]	abs. error [%]
C	6	7.37	15.91	23.58	2.33
N	7	1.14	2.47	3.14	0.46
O	8	19.85	42.86	47.68	6.20
Si	14	13.80	29.79	18.88	1.92
Pt	78	0.00	0.00	0.00	0.00
Na	11.00	2.72	5.87	4.54	0.46
Mg	12	0.8	1.76	1.29	0.12
Al	13	0.62	1.34	0.89	0.09
		46.32	100.00	100.00	



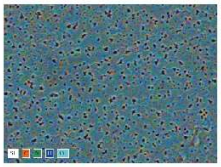
[Glass-PI] PI side after peel test



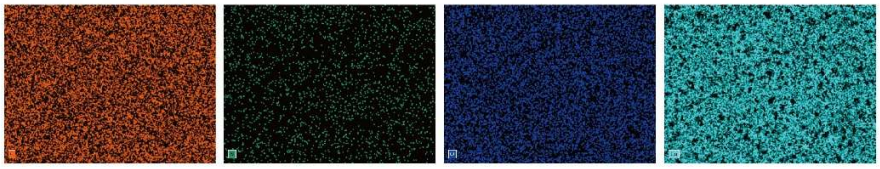
Element	At. No.	Mass [%]	ss Norm.	Atom [%]	abs. error [%]
C	6	61.76	61.76	68.10	18.91
N	7	2.65	2.65	2.51	1.04
O	8	35.40	35.40	29.30	11.07
Si	14	0.19	0.19	0.09	0.03
Pt	78	0.00	0.00	0.00	0.00
		100.00	100.00	100.00	



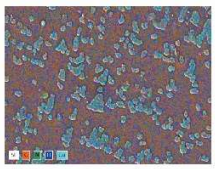
(c) [Cu-PI] Cu side after peel test



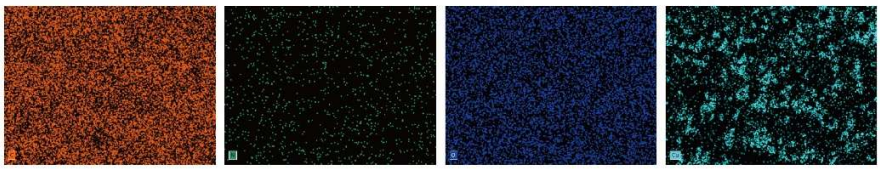
Element	At. No.	Mass [%]as Norm.	Atom [%]abs. error [%]		
C	6	20.56	20.56	46.10	6.94
O	8	12.44	12.44	21.85	4.90
Ti	22	2.96	2.96	1.74	0.31
Cu	29	64.04	64.04	28.31	20.55
Pt	78	0.00	0.00	0.00	0.00
		100.00	100.00	100	



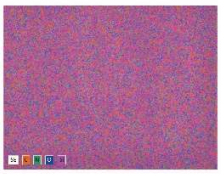
[Cu-PI] PI side after peel test



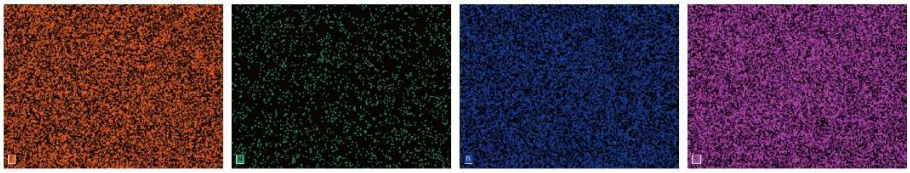
Element	At. No.	Mass [%]as Norm.	Atom [%]abs. error [%]		
C	6	64.36	64.36	72.67	20.92
O	8	31.10	31.10	26.36	12.64
Cu	29	4.54	4.54	0.97	1.96
Pt	78	0.00	0.00	0.00	0.00
		100.00	100.00	100.00	



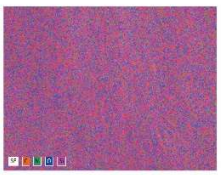
(d) [PDMS-PI] PDMS side after peel test



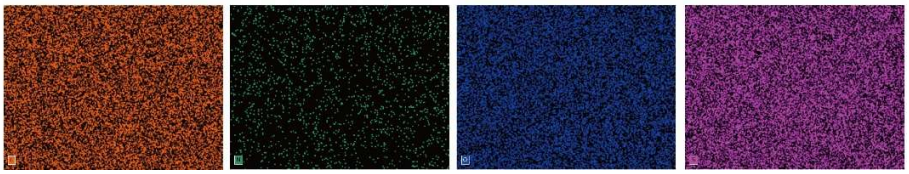
Element	At. No.	Mass [%]as Norm.	Atom [%]abs. error [%]		
C	6	36.04	36.04	36.85	10.15
N	7	21.18	21.18	21.85	17.33
O	8	42.53	42.53	28.40	15.77
Si	14	5.65	5.65	2.90	0.69
Pt	78	0.00	0.00	0.00	0.00
		100.00	100.00	100.00	



[PDMS-PI] PI side after peel test

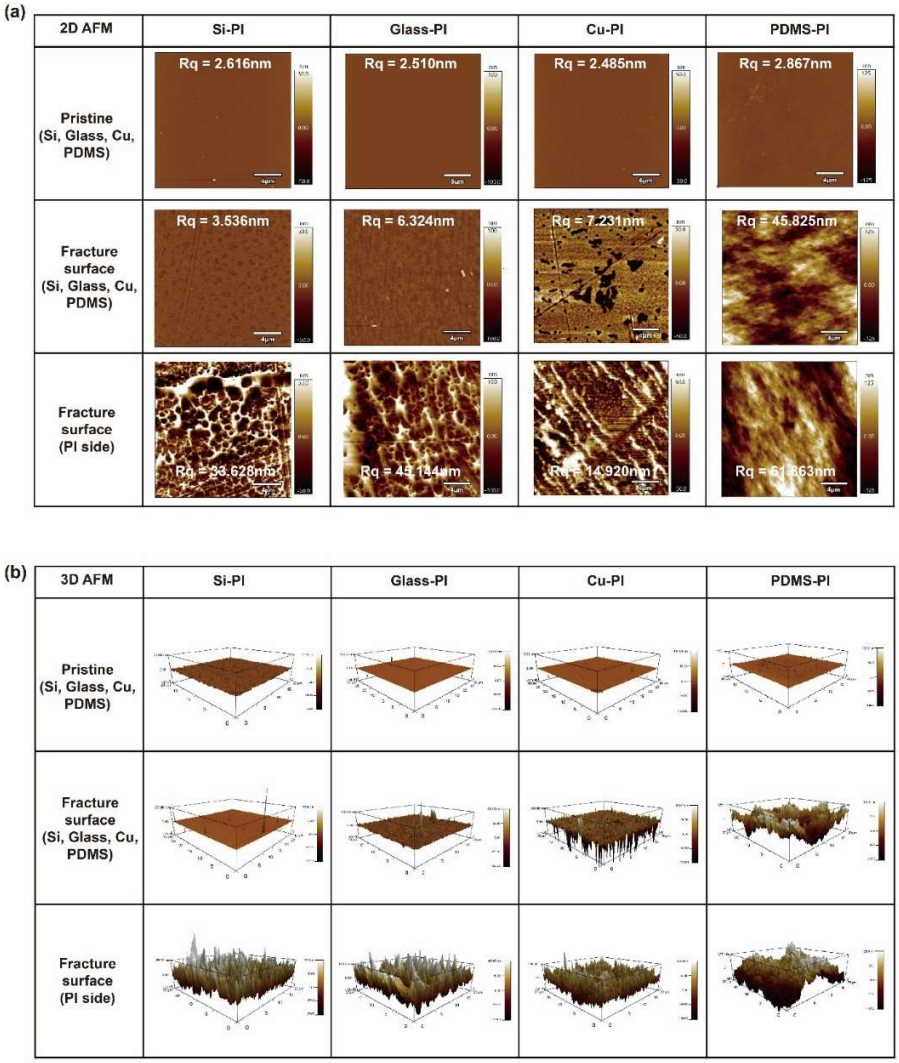


Element	At. No.	Mass [%]as Norm.	Atom [%]abs. error [%]		
C	6	36.04	36.04	43.53	12.01
N	7	10.15	10.15	10.52	12.07
O	8	46.56	46.56	42.22	17.34
Si	14	7.24	7.24	3.74	0.89
Pt	78	0.00	0.00	0.00	0.00
		100.00	100.00	100.00	



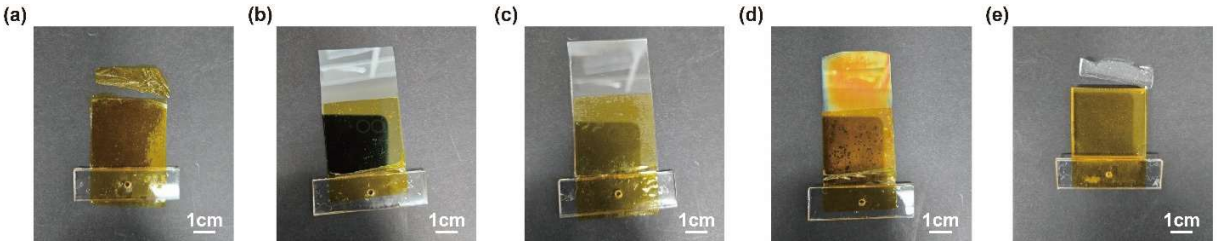
Supplementary Fig. 22 | EDS analysis of fracture surfaces after peeling of heterogeneous interfaces.

Representative EDS elemental maps and corresponding elemental compositions of the opposing fracture surfaces obtained after 90° peel tests of (a) Si–PI, (b) glass–PI, (c) Cu–PI and (d) PDMS–PI interfaces. For the Si–PI, glass–PI and Cu–PI interfaces, elemental signatures associated with the opposing material are detected on selected fracture surfaces, consistent with the material transfer observed by SEM in Fig. 5c–e. For PDMS–PI, a pronounced Si-rich signal is detected on the PI-side fracture surface, consistent with residual PDMS resulting from cohesive fracture within the PDMS rather than interfacial separation. These EDS results support the material-transfer and cohesive-failure modes identified from the corresponding fracture-surface morphologies.



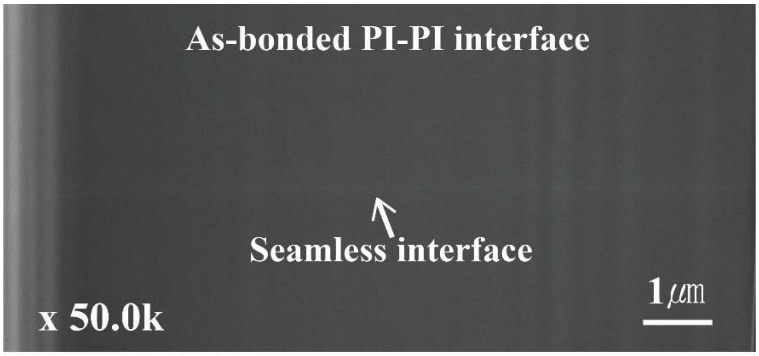
Supplementary Fig. 23 | AFM topography and surface roughness of heterogeneous interfaces before and after peeling.

(a) Representative 2D AFM height images of pristine Si, glass, Cu and PDMS substrates and the corresponding substrate-side and PI-side fracture surfaces after 90° peel tests of Si–PI, glass–PI, Cu–PI and PDMS–PI interfaces. The root-mean-square surface roughness, R_q, is indicated in each image. The pristine Si, glass, Cu and PDMS surfaces exhibit R_q values of 2.616, 2.510, 2.485 and 2.867 nm, respectively, which increase after peeling to 3.536, 6.324, 7.231 and 45.825 nm on the corresponding substrate-side fracture surfaces. The PI-side fracture surfaces exhibit R_q values of 33.628, 45.144, 14.920 and 61.863 nm for Si–PI, glass–PI, Cu–PI and PDMS–PI, respectively, substantially exceeding that of pristine PI ($R_q = 6.357$ nm). (b) Corresponding 3D AFM topographies. The increased roughness and topographic heterogeneity after peeling are consistent with the substrate-dependent deformation and failure modes observed in the corresponding fracture-surface SEM images in Fig. 5c–f.



Supplementary Fig. 24 | Failure states of molecularly bridged interfaces after macroscopic load-bearing tests.

Representative photographs of (a) PI–PI, (b) Si–PI, (c) glass–PI, (d) Cu–PI and (e) PDMS–PI specimens after the weight-supporting tests shown in Fig. 5g,h. The bonded regions remained intact after loading. In the PI–PI and PDMS–PI specimens, failure occurred within the constituent PI and PDMS materials, respectively, rather than by separation of the bonded interface.



Supplementary Fig. 25 | Cross-sectional FIB–SEM image of the as-bonded PI–PI interface before reliability testing.

Representative cross-sectional FIB–SEM image of the N_{22}-bonded PI–PI interface before thermal cycling and water immersion. The as-bonded interface exhibits continuous structural contact without obvious interfacial gaps or delamination and serves as the baseline for comparison with the interfaces after environmental exposure shown in Fig. 6c.

Fig. 1d label	SI Ref.	System	Thickness, t (m)	Interfacial fracture energy, G_c (J m^{-2})	Classification
1	1	PAAm–alginate hydrogel/glass	3.00E-03	1500	Chemical-bond-mediated
11	2	TMOS-modified Si/Si	4.00E-09	2	Chemical-bond-mediated
27a	3	O_2-plasma-activated SiO_2/SiO_2	2.00E-09	2	Chemical-bond-mediated
27b	3	O_2-plasma-activated SiO_2/SiO_2	1.00E-07	2.35	Chemical-bond-mediated
28	4	Thermal SiO_2/PECVD SiO_2	6.00E-08	2.63	Chemical-bond-mediated
29	5	InP/Si	1.50E-09	0.63	Chemical-bond-mediated
30a	6	BCB/SiO_2 with adhesion promoter	4.00E-07	19	Chemical-bond-mediated
30b	6	BCB/SiO_2 with adhesion promoter	2.60E-06	31	Chemical-bond-mediated
31a	7	Si/ACF	3.50E-05	2.16	Physical-interaction-mediated
31b	7	FR-4/ACF	3.50E-05	415	Physical-interaction-mediated
32	8	PBA-based model PSA/polyester	1.50E-03	33.9	Physical-interaction-mediated
33	9	3M 810 acrylic PSA/release-coated backing	2.80E-05	4	Physical-interaction-mediated
34	10	3M Scotch 600 PSA/release-coated backing	2.00E-05	50	Physical-interaction-mediated
35	11	SIS/SI model PSA/glass	1.50E-04	801	Physical-interaction-mediated
36	12	pLCE ionic nanomesh/glass	8.00E-06	370	Physical-interaction-mediated
37	13	Heterogeneous P(BA-co-AA) network/acrylate	3.00E-04	50	Physical-interaction-mediated
38	14	BTIM/porcine skin	2.00E-03	300	Chemical-bond-mediated
39	15	PVA hydrogel/glass	1.00E-04	7500	Physical-interaction-mediated
40	16	PAA brush/PAAm hydrogel on natural rubber	5.00E-05	135	Physical-interaction-mediated
41	17	DNR PAA hydrogel/wet porcine skin	1.00E-03	500	Physical-interaction-mediated
42	18	PDA@OHG /steel	7.00E-04	189	Physical-interaction-mediated

This work	PI-PI	3.20E-09	500	Interlinked molecular bridge
	Si-PI	3.20E-09	160	Interlinked molecular bridge
	glass-PI	3.20E-09	114	Interlinked molecular bridge
	Cu-PI	3.20E-09	311	Interlinked molecular bridge
	PDMS-PI	3.20E-09	456	Interlinked molecular bridge

Supplementary Table 1 | Literature data used to construct the Ashby plot of adhesive/interphase thickness and interfacial fracture energy in Fig. 1d.

The adhesive/interphase thickness (t) and corresponding interfacial fracture or adhesion energy, denoted as G_c for comparison, were compiled from the cited studies. Systems were classified as chemical-bond-mediated or physical-interaction-mediated according to the dominant interfacial attachment mechanism. Letter suffixes indicate different material or thickness conditions reported in the same reference.

Amino-terminated silane, A_x	Glycidyl-terminated silane, G_y	Interlinked molecular bridge, Nz
A_9	G_9	N_{19}
A_{12}	G_9	N_{22}
A_{17}	G_9	N_{27}
A_{24}	G_9	N_{34}
A_9	G_{14}	N_{24}
A_{12}	G_{14}	N_{27}
A_{17}	G_{14}	N_{32}
A_{24}	G_{14}	N_{39}

Supplementary Table 2 | Silane combinations used to form interlinked molecular bridges.

A_x and G_y denote amino- and glycidyl-silane chains containing x and y backbone bonds, respectively. Epoxy–amine coupling between complementary chains forms an interlinked molecular bridge, N_z, containing z backbone bonds, where $z = x + y + 1$. The additional bond corresponds to the newly formed C–N bond. Bond counts were defined along the continuous load-bearing covalent backbone. N_{27} was prepared using both A_{17}/G_9 and A_{12}/G_{14} combinations. The two combinations showed comparable mean interfacial fracture energies and were pooled for the N_{27} value reported in Fig. 2e.

Supplementary Table 3 | Force–separation results for the simulated molecular interfaces.

Maximum traction, F_{max}, critical separation, δ_c, separation work, W_{sep}, and normalized separation work are listed for each bridge length and nominal brush density. Values are reported as the mean ± standard deviation from three separation trajectories initiated from the same equilibrated molecular configuration using different velocity seeds. The normalized separation work was calculated relative to the mean W_{sep} of the N_{39}, ρ_H model.

	Maximum traction, F_{max} (nN)		Critical separation δ_c (Å)		Work of separation W_{sep} (J/m^2)		Normalized Work of separation	
			ρ_L = 1.96 sites nm^{-2}					
N_{19}	92.30	±8.89	17.47	±0.24	5.76	±0.48	0.29	±0.02
N_{22}	54.02	±7.17	38.97	±1.55	6.36	±0.62	0.32	±0.03
N_{24}	53.08	±6.99	36.75	±1.01	6.47	±0.48	0.32	±0.02
N_{27}	51.92	±9.23	40.47	±1.76	6.68	±1.25	0.33	±0.06
N_{32}	49.62	±5.79	48.60	±4.08	7.01	±0.59	0.35	±0.03
N_{34}	105.83	±5.14	25.83	±0.79	8.90	±0.40	0.44	±0.02
N_{39}	62.85	±8.37	53.33	±3.54	9.64	±0.80	0.48	±0.04
			ρ_H = 3.92 sites nm^{-2}					
N_{19}	184.00	±16.27	16.88	±0.10	10.43	±1.20	0.52	±0.06
N_{22}	212.60	±30.52	15.75	±0.10	12.58	±1.62	0.62	±0.08
N_{24}	161.57	±7.00	30.00	±1.14	13.97	±0.82	0.69	±0.04
N_{27}	139.41	±10.54	30.92	±0.42	14.59	±0.64	0.72	±0.03
N_{32}	142.56	±2.98	42.67	±1.24	18.18	±1.02	0.90	±0.05
N_{34}	173.78	±1.24	35.92	±1.20	18.27	±1.24	0.91	±0.06
N_{39}	146.90	±29.54	44.83	±1.74	20.13	±3.10	1.00	±0.15

Supplementary Note 1 | Contribution of PI peel-arm deformation to the measured fracture energy

The possible contribution of deformation of the PI peel arm to the measured fracture energy was evaluated for the 90° peel geometry. During peeling, the 25-μm-thick PI film undergoes pronounced bending near the peel front. However, the peeled film recovers its original flat configuration after complete unloading without apparent permanent curvature (Supplementary Fig. 5), indicating that the macroscopic bending deformation is predominantly elastic and recoverable.

The contribution of axial extension of the peel arm was further quantified using the Kendall peel model. For an extensible peel arm, the energy release rate is given by

$$G = \frac{P}{b}(1 - \cos\theta) + \frac{P^2}{2b^2Et},$$

where $P$is the peel force, $b$is the specimen width, $\theta$is the peel angle, $E$is the Young's modulus of the peel arm and $t$is its thickness. For the 90° peel geometry used in this study, $\theta = 90°$, giving

$$G = \frac{P}{b} + \frac{P^2}{2b^2Et}.$$

The second term represents the correction associated with elastic axial extension of the peel arm. For the N32 interface, the measured peel force corresponds to $P/b \approx 500\text{N m}^{-1}$. Using a PI thickness of 25 μm and a Young's modulus of approximately 3.0 GPa, the extensibility contribution is

$$G_{\text{ext}} = \frac{(500\ \text{N m}^{-1})^2}{2(3.0 \times 10^9\ \text{Pa})(25 \times 10^{-6}\ \text{m})} \approx 1.7\ \text{J m}^{-2}.$$

This value corresponds to approximately 0.3% of the measured fracture energy of $\sim 500\text{J m}^{-2}$. Together with the complete macroscopic recovery of the PI peel arm after unloading, these results indicate that deformation of the thin PI peel arm makes only a minor contribution to the exceptionally high fracture energy measured for the molecularly bridged interface.

Supplementary Note 2 | Calculation of substrate-corrected elemental ratios and the Si^{4+}/Si^{0} ratio

The surface atomic concentrations of C, N, O and Si were obtained from XPS survey spectra using the relative sensitivity factors implemented in MultiPak. To minimize variations arising from attenuation of the Si substrate signal, the carbon and nitrogen concentrations of each silane-functionalized surface were normalized to the corresponding Si concentration. For an element X, where $X = \mathrm{C}$ or N, the normalized elemental ratio was calculated as

$$\left(\frac{X}{\mathrm{Si}}\right)_i = \frac{x_{X,i}}{x_{\mathrm{Si},i}}, \qquad \text{(S1)}$$

where $x_{X,i}$ and $x_{\mathrm{Si},i}$ are the survey-derived atomic percentages of element X and Si, respectively, for sample i.

To account for adventitious carbon and other background contributions present on the untreated Si wafer, the corresponding ratio measured on bare Si was subtracted from that of each silane-functionalized surface:

$$\Delta\left(\frac{X}{\mathrm{Si}}\right)_i = \left(\frac{X}{\mathrm{Si}}\right)_i - \left(\frac{X}{\mathrm{Si}}\right)_{\text{bare Si}}, \; X = \mathrm{C} \text{ or } \mathrm{N}. \qquad \text{(S2)}$$

Accordingly, $\Delta(\mathrm{C/Si})$ and $\Delta(\mathrm{N/Si})$ represent the increases in the Si-normalized carbon and nitrogen signals relative to the bare-Si reference. The total Si concentration was reported directly as the survey-derived atomic percentage and was not corrected by subtraction of the bare-Si value. The relative contributions of substrate and oxidized Si were determined from the high-resolution Si 2p spectra. A Shirley background was subtracted before peak fitting, and the Si 2p components were fitted using Gaussian–Lorentzian line-shape functions. Identical background-subtraction and peak-fitting conditions were applied across the Si sample series. The Si^{0} component was assigned to elemental Si originating from the crystalline Si wafer substrate. By contrast, the higher-binding-energy Si^{4+} component was assigned to oxidized Si species associated with the surface layer, including the native Si oxide and silane-derived Si–O–Si or Si–O–substrate structures. The Si^{4+}/Si^{0} ratio was then calculated from the integrated areas of the fitted components:

$$\frac{\mathrm{Si}^{4+}}{\mathrm{Si}^{0}} = \frac{A_{\mathrm{Si}^{4+}}}{A_{\mathrm{Si}^{0}}}, \qquad \text{(S3)}$$

where $A_{\mathrm{Si}^{4+}}$ is the integrated area of the oxidized-Si component associated with the surface oxide and silane-containing overlayer, and $A_{\mathrm{Si}^{0}}$ is the integrated area of the elemental crystalline-Si component originating from the underlying Si wafer. Because both components arise from the Si 2p core level, the ratio was calculated directly from their fitted peak areas. An increase in $\mathrm{Si}^{4+}/\mathrm{Si}^{0}$ therefore indicates an increased contribution from the oxidized surface layer relative to the crystalline Si substrate.

The Si^{4+}/component includes contributions from both the native oxide and silane-derived Si–O species. However, all Si specimens were subjected to identical pretreatment and storage conditions; the native-oxide contribution was therefore regarded as a common baseline across the sample series. Accordingly, differences in the Si^{4+}/Si^{0} ratio were interpreted primarily as relative changes

in the silane-associated oxidized surface layer. The ratio was used as a comparative indicator of surface-layer formation rather than as a direct or absolute measure of silane coverage.

Supplementary Note 3 | Estimation of XPS-derived silane-layer and interphase thicknesses

The effective thicknesses of the silane-associated surface layers formed on Si were estimated from the fitted Si 2p spectra using the overlayer-thickness module implemented in MultiPak. The Si^{4+} component was assigned to the oxidized surface region, including the native Si oxide and silane-associated Si–O species, whereas the Si^0 component originated from the underlying crystalline Si substrate. Attenuation of the substrate photoelectron signal by the surface layer was analyzed using an established overlayer model for quantitative XPS analysis.[19]
The apparent overlayer thickness was calculated as

$$d = \lambda \sin\theta \ln\left[\alpha\left(\frac{I_\mathrm{F} + I_\mathrm{S}\mathrm{OV}}{I_\mathrm{S} - I_\mathrm{F}\mathrm{OV}}\right) + 1\right], \qquad \text{(S4)}$$

where d is the apparent overlayer thickness, λ is the attenuation-length parameter for Si 2p photoelectrons travelling through the surface layer, and θ is the photoelectron take-off angle relative to the sample plane. I_F and I_S are the integrated intensities of the film-associated Si^{4+} and substrate Si^0 components, respectively. The factor α accounts for differences in the relative sensitivity of the film and substrate signals, whereas OV is the correction parameter for spectral overlap between the two components.
Because the Si^{4+} and Si^0 components were obtained from the same Si 2p core level, α was set to 1. The overlap-correction parameter was set to $\mathrm{OV} = 0$ because the Si^{4+} and Si^0 contributions were independently determined by peak fitting. Under these conditions, equation (S4) reduces to $d = \lambda \sin\theta \ln(1 + I_\mathrm{F}/I_\mathrm{S})$. A photoelectron take-off angle of 45° was used.

Predictive determination of the attenuation-length parameter
The attenuation-length parameter was estimated using the TPP-2M predictive equation developed by Tanuma, Powell and Penn.[20,21] The TPP-2M model provides a generalized predictive estimate of the electron inelastic mean free path for materials for which experimentally derived optical-loss data are unavailable. [20,21] The predicted IMFP, λ_TPP, is expressed as

$$\lambda_\mathrm{TPP} = \frac{E}{E_\mathrm{p}^2\left[\beta\ln(\gamma E) - \frac{C}{E} + \frac{D}{E^2}\right]}, \qquad \text{(S5)}$$

where E is the photoelectron kinetic energy and E_p is the free-electron plasmon energy. The plasmon energy is defined as

$$E_\mathrm{p} = 28.8\left(\frac{N_\mathrm{v}\rho}{M}\right)^{1/2}, \qquad \text{(S6)}$$

and the material-dependent parameters are given by

$$\beta = -0.10 + \frac{0.944}{\left(E_{\mathrm{p}}^2 + E_{\mathrm{g}}^2\right)^{1/2}} + 0.069\rho^{0.1},$$
$$\gamma = 0.191\rho^{-0.5},$$
$$C = 1.97 - 0.91U,$$
$$D = 53.4 - 20.8U,$$
$$U = \frac{N_{\mathrm{v}}\rho}{M}, \qquad \text{(S7)}$$

where N_{v} is the number of valence electrons per molecule, M is the molecular weight, ρ is the layer density and E_{g} is the bandgap energy. [20,21]

For Al Kα excitation, the kinetic energy of the Si 2p photoelectrons was approximately 1,387 eV. The molecular weights and valence-electron counts were calculated from the molecular compositions of the amino- and glycidyl-terminated silanes. Because the density and bandgap of the grafted organic–siloxane layers could not be independently determined, representative values of $\rho = 1.05$ g cm^{-3} and $E_{\mathrm{g}} = 5$ eV were applied consistently across the molecular series.

The TPP-2M-predicted IMFPs ranged from approximately 3.94 to 4.00 nm across the silane series. Accordingly, $\lambda = 4.0$ nm was used as a common attenuation-length parameter for the subsequent MultiPak thickness calculations.

The TPP-2M-derived value represents a generalized predictive IMFP rather than a specimen-specific, experimentally measured effective attenuation length.[19-21] The effective attenuation length used in quantitative XPS analysis may differ from the IMFP because it additionally reflects elastic-scattering and measurement-geometry effects.[19] The calculated values are therefore reported as XPS-derived effective thicknesses rather than exact physical dimensions of individual grafted molecules.

XPS-derived effective silane-layer thicknesses

All Si specimens were subjected to identical pretreatment and storage conditions. The contribution of the native oxide to the Si^{4+} signal was therefore regarded as a common baseline across the sample series. Nevertheless, because the Si^{4+} envelope contains contributions from both the native oxide and silane-associated Si–O species, the calculated values were interpreted as comparative, attenuation-equivalent surface-layer thicknesses rather than absolute silane-film thicknesses.

Using $\lambda = 4.0$ nm, the XPS-derived effective thickness was approximately 0.82 nm for A_9, increased to 1.99 and 2.55 nm for A_{12} and A_{17}, respectively, and decreased to approximately 1.16 nm for A_{24}. The corresponding effective thicknesses of the glycidyl-terminated layers were approximately 0.54 nm for G_9 and 0.68 nm for G_{14}.

The increase from A_9 to A_{17} is consistent with the increasing molecular dimensions of the aminosilanes. Despite its greater contour length, A_{24} exhibited a lower area-averaged effective thickness. Together with the AFM observations in Fig. 3, this behaviour is consistent with molecular coiling and island-like aggregation, in which locally thicker assemblies occupy only part of the substrate surface rather than forming a laterally uniform extended layer.

Effective thickness of the N_{32} molecular interphase

The N_{32} bridge was formed through coupling between A_{17} and G_{14}, which produced the maximum adhesion response in the present molecular series. The combined XPS-derived effective thickness of the complementary surface layers was estimated as

$$
\begin{aligned}
d_{\mathrm{N}_{32},\mathrm{eff}} &= d_{\mathrm{A}_{17}} + d_{\mathrm{G}_{14}} \\
&= 2.55\ \mathrm{nm} + 0.68\ \mathrm{nm} \\
&\approx 3.23\ \mathrm{nm}.
\end{aligned}
\qquad \text{(S8)}
$$

This value represents the combined attenuation-equivalent thicknesses of the independently functionalized surfaces before bonding and is not a direct cross-sectional measurement of the assembled interface. Molecular interpenetration, tilt and conformational rearrangement during bonding may further reduce the surface-normal separation between the opposing substrates.

A simple C–C-equivalent estimate of the 32-bond load-bearing path, 32×0.154 nm, gives a hypothetical fully extended contour-length scale of approximately 4.9 nm. This calculation is intended only as a molecular-length estimate because the load-bearing path also contains C–N, C–O, Si–C and Si–O bonds and does not adopt a perfectly linear conformation. Because the actual surface-normal thickness is reduced by bond angles, molecular tilt and conformational rearrangement, the covalently bridged adhesive layer is described conceptually as a sub-5-nm molecular interphase. For quantitative comparisons, including the adhesion performance map, the XPS-derived effective thickness of approximately 3.2 nm was used.

Supplementary References

1. Yuk, H., Zhang, T., Lin, S., Parada, G. A. & Zhao, X. Tough bonding of hydrogels to diverse non-porous surfaces. *Nat. Mater.* **15**, 190–196 (2016).

2. Gösele, U., Steinnkirchner, J., Martini, T., Reiche, M. & Kästner, G. Silicon wafer bonding vi a designed monolayers. *Adv. Mater.* **7**, 662–665 (1995).

3. Olbrechts, B., Zhang, X., Bertholet, Y., Pardoen, T. & Raskin, J.-P. Effect of interfacial SiO_2 thickness for low temperature O_2 plasma activated wafer bonding. *Microsyst. Technol.* **12**, 383–390 (2006).

4. Liang, D. et al. Low-temperature, strong SiO_2–SiO_2 covalent wafer bonding for III–V compound semiconductors-to-silicon photonic integrated circuits. *J. Electron. Mater.* **37**, 1552–1559 (2008).

5. Tong, Q.-Y., Gan, Q., Hudson, G., Fountain, G. & Enquist, P. Low temperature InP/Si wafer bonding. *Appl. Phys. Lett.* **84**, 732–734 (2004).

6. Kwon, Y., Seok, J., Lu, J. Q., Cale, T. S. & Gutmann, R. J. Critical adhesion energy of benzocyclobutene-bonded wafers. *J. Electrochem. Soc.* **153**, G347–G352 (2006).

7. Sim, G. D., Chung, C. K., Paik, K. W. & Lee, S. B. Moisture induced interface weakening in ACF package. *Mater. Sci. Eng. A* **528**, 698–705 (2010).

8. Wan, Y., Yin, Q., Zhang, P., Yang, C. & Bai, R. Interfacial fatigue fracture of pressure sensitive adhesives. *Extreme Mech. Lett.* **72**, 102248 (2024).

9. Grzelka, M., Kooij, S., Woutersen, S., Adda-Bedia, M. & Bonn, D. Transition from viscoelastic to fracture-like peeling of pressure-sensitive adhesives. *Soft Matter* **18**, 999–1004 (2022).

10. Villey, R. et al. Rate-dependent elastic hysteresis during the peeling of pressure sensitive adhesives. *Soft Matter* **11**, 3480–3491 (2015).

11. Pandey, V., Fleury, A., Villey, R., Creton, C. & Ciccotti, M. Linking peel and tack performances of pressure sensitive adhesives. *Soft Matter* **16**, 3267–3275 (2020).

12. Du, Q. et al. Self-compliant ionic nanomesh for gas-permeable and stress-free on-skin electronics. *Nat. Commun.* **16**, 11510 (2025).

13. Zhang, P., Ruan, H., Li, Q., He, Y. & Yang, C. Resolving hyperelasticity-adhesiveness conflict in polymer networks by in situ constructing mechanical heterogeneities. *Nat. Commun.* **16**, 6094 (2025).

14. Yang, Q. et al. Photocurable bioresorbable adhesives as functional interfaces between flexible bioelectronic devices and soft biological tissues. *Nat. Mater.* **20**, 1559–1570 (2021).

15. Liu, J. et al. Fatigue-resistant adhesion of hydrogels. *Nat. Commun.* **11**, 1071 (2020).

16. Wang, Y. et al. Instant, tough, noncovalent adhesion. *ACS Appl. Mater. Interfaces* **11**, 40749–40757 (2019).

17. Yi, B. et al. Surface hydrophobization of hydrogels via interface dynamics-induced network reconfiguration. *Nat. Commun.* **15**, 239 (2024).

18. Xie, W. et al. Organohydrogel-based transparent terahertz absorber via ionic conduction loss. *Nat. Commun.* **15**, 38 (2024).

19. Jablonski, A. & Powell, C. J. The electron attenuation length revisited. *Surf. Sci. Rep*. **47**, 33–91 (2002).

20. Tanuma, S., Powell, C. J. & Penn, D. R. Calculations of electron inelastic mean free paths. V. Data for 14 organic compounds over the 50–2000 eV range. *Surf. Interface Anal.* **21**, 165–176 (1994).

21. Tanuma, S., Powell, C. J. & Penn, D. R. Calculation of electron inelastic mean free paths (IMFPs). VII. Reliability of the TPP-2M IMFP predictive equation. *Surf. Interface Anal*. **35**, 268–275 (2003).

Supplementary Movie 1 | Representative 90° peel tests of plasma-only interface.

Representative 90° peel tests of plasma-only interface, displayed together with the corresponding peel force–displacement curves recorded during testing.

Supplementary Movie 2 | Representative 90° peel tests of N_{32}-bonded PI–PI interfaces.

Representative 90° peel tests of N_{32}-bonded PI–PI interface, displayed together with the corresponding peel force–displacement curves recorded during testing.